Published in final edited form as:
Neuroimage. 2012 April 2; 60(2): 1412–1425. doi:10.1016/j.neuroimage.2012.01.056.

Ball and Rackets: Inferring Fibre Fanning from Diffusion-weighted MRI

Stamatios N. Sotiropoulos[a,*], **Timothy E. Behrens**[a], and **Saad Jbabdi**[a]
[a]FMRIB Centre, University of Oxford, John Radcliffe Hospital, Headington, UK

Abstract

A number of methods have been proposed for resolving crossing fibres from diffusion-weighted (DW) MRI. However, other complex fibre geometries have drawn minimal attention. In this study, we focus on fibre orientation dispersion induced by within-voxel fanning. We use a multi-compartment, model-based approach to estimate fibre dispersion. Bingham distributions are employed to represent continuous distributions of fibre orientations, centred around a main orientation, and capturing anisotropic dispersion. We evaluate the accuracy of the model for different simulated fanning geometries, under different acquisition protocols and we illustrate the high SNR and angular resolution needs. We also perform a qualitative comparison between our parametric approach and five popular non-parametric techniques that are based on orientation distribution functions (ODFs). This comparison illustrates how the same underlying geometry can be depicted by different methods. We apply the proposed model on high-quality, post-mortem macaque data and present whole-brain maps of fibre dispersion, as well as exquisite details on the local anatomy of fibre distributions in various white matter regions.

Keywords

Diffusion MRI; white matter; parametric deconvolution; fibre fanning; fibre bending; Bingham distribution; macaque

1. Introduction

Diffusion-weighted magnetic resonance imaging (DW-MRI) utilizes the random, thermally-driven motions of water molecules as a contrast mechanism (Le Bihan et al., 1986). In the brain, diffusion is restricted and hindered by the various tissue processes and can therefore be used to probe microstructure. Diffusion tensor imaging (DTI) (Basser et al., 1994) allowed a formal description of this relation. Elongated diffusion profiles can be revealed in regions with coherent structure, such as brain white matter, where preferred directions of diffusion displacements coincide with the major fibre orientations (Pierpaoli et al., 1996). Following these local orientation estimates allows in-vivo reconstruction of fibre bundles via tractography approaches (Conturo et al., 1999; Mori et al., 1999; Basser et al., 2000).

*Corresponding author: stam@fmrib.ox.ac.uk (Stamatios N. Sotiropoulos).

Despite its success in delineating many major white matter bundles (Catani et al., 2002), DTI-based tractography has limitations arising from the tensor model assumptions. DTI orientation estimates have a direct biophysical meaning only when a single bundle of parallel axons runs through a voxel of the image. Interpretation of the model estimates for more complex patterns, such as within-voxel fibre crossing, kissing, bending or fanning, is less straightforward (Basser et al., 2000; Seunarine and Alexander, 2009). More sophisticated approaches have therefore been developed.

It has been almost a decade since the first attempts to resolve complex fibre architectures from DW-MRI (Tuch et al., 2002). Both parametric and non-parametric approaches have been introduced, where characterisation of fibre *crossing* has drawn much more attention than other patterns (Seunarine and Alexander, 2009). Tuch et al described the extension of the diffusion tensor model to a multi-tensor decomposition of the signal, acknowledging the identifiability issues of this approach (Tuch et al., 2002). More identifiable variants have been proposed since then, with the inclusion of geometric (Alexander, 2005; Kreher et al., 2005; Peled et al., 2006; Behrens et al., 2007) or spatial constraints (Sotiropoulos et al., 2008; King et al., 2009). A direct extension of the multi-tensor model to a continuous domain is the recent notion of the tensor distribution function (Leow et al., 2009). Other parametric approaches include multi-compartment estimation with consideration of restriction effects (Assaf and Basser, 2005) and orientation estimation through diffusion kurtosis models (Lazar et al., 2008).

Non-parametric approaches have primarily focused on the estimation of *diffusion* or *fibre* orientation distribution functions (dODFs / fODFs). dODFs represent the orientations of preferred diffusion displacements. They can be obtained from the measured signal either through radial integration of the estimated diffusion scatter pattern (Wedeen et al., 2005) or through a Funk-Radon transform of the signal (Tuch, 2004; Descoteaux et al., 2007) and functions of it (Aganj et al., 2010). fODFs more directly represent the *continuous* distribution of fibre orientations and are estimated through deconvolution approaches (Tournier et al., 2004; Alexander, 2005; Anderson, 2005; Dell'Acqua et al., 2007; Descoteaux et al., 2009; Patel et al., 2010; Yeh et al., 2011). Deconvolution is utilized in PASMRI as well (Jansons and Alexander, 2003) to estimate a function on the sphere that captures the persistent angular structure of the diffusion scatter pattern. Other types of non-parametric approaches use variants of the dODF, such as the diffusion orientation transform (Ozarslan et al., 2006) and the spin distribution function (Yeh et al., 2010).

All the above model-based (mixture of tensors) and model-free (ODFs) approaches were primarily designed or evaluated for resolving fibre *crossings*. Indeed, they were used for detecting *discrete* sets of fibre orientations assuming that they align with locally (in terms of angular orientation) minimal hindrance to diffusion. In most of the model-based cases, these directions are explicitly included in the model and estimated from the data. In the case of model-free approaches, they are estimated using post-processing steps that detect local maxima in the ODFs.

Incorporating information on (discrete) crossing fibres has significantly improved tractography reconstructions. Algorithms that allow for more than a single fibre orientation per voxel are more sensitive to detecting secondary white matter bundles that cross larger ones (Behrens et al., 2007). However, other complex patterns of intra-voxel axonal organisation still pose challenges to modern tractography. For example, many white matter fibre bundles appear to have a fanning geometry (e.g. corona radiata). At the voxel-level, these fanning geometries indicate that axons do not follow a discrete set of orientations, but a continuum, potentially centred on a mean orientation. Of particular interest is the case where fanning is anisotropic, i.e. more pronounced along one orientation than others. As

discussed in (Jbabdi and Johansen-Berg, 2011), tractography algorithms can potentially gain sensitivity if they were to use an accurate estimate of fanning rather than a set of discrete peaks in the fODF.

Some of the model-free approaches described above indeed attempt at reconstructing a continuous fODF, potentially capturing fanning geometries. Seunarine et al have pointed out that these functions may exhibit stretched peaks in the presence of anisotropic fanning or bending (Seunarine et al., 2007). However, the shape of the peaks (their broadness) is not necessarily an accurate description of the precise fanning of underlying axonal fibres. In general, fODFs are obtained through deconvolution approaches (Tournier et al., 2004) or ad-hoc sharpening of the dODF (Tuch, 2004). While reconstruction steps may not affect the location of the peak orientations (used in current tractography), they may affect the shape of the fODF. For example, the regularization method (Tournier et al., 2007) or the truncation order of the basis used in a spherical deconvolution approach may affect the broadness of the fODF (Tournier et al., 2004; Anderson, 2005); also multiple peaks may be detected where in fact the underlying geometry is one of fibre fanning (Nedjati-Gilani and Alexander, 2009).

A very limited number of parametric approaches have focused on fanning patterns. A model-based deconvolution of the signal using Bingham and Watson distributions is described in (Kaden et al., 2007). Fanning is explicitly modelled, but the study focused on the reduction in propagated uncertainty with this approach, when tracking using the main orientation of the fanning compartment. A different model that is based on the generation of subvoxel fanning/bending grids is presented in (Nedjati-Gilani and Alexander, 2009) and preliminary results on inferring a single fanning population are shown. An approach to quantify intravoxel fibre dispersion, caused by either crossing or fanning, has been recently presented, that is based on the autocorrelation function of the spherical signal or features of it, such as the ODF (Assemlal et al., 2011).

Another group of methods utilize neighborhood information to infer fanning. A curve inference framework on fibre orientation estimates has been presented by (Savadjiev et al., 2008) to differentiate between spatial patterns of fanning and crossing. Scalar indices of fanning and curving were defined in (Savadjiev et al., 2010) using spatial gradients of diffusion tensor fields. These approaches have exhibited promising results, but they might have benefitted more if local mapping of fanning information were available in each voxel.

Here, we take a model-based approach to the problem. We explicitly model the effect of fibre fanning on the diffusion signal using a parametric spherical ODF. We are extending the ball & stick model (Behrens et al., 2003, 2007) and use Bingham distributions to perform the deconvolution. Our model is a special case of the one introduced by (Kaden et al., 2007), however by choosing a “stick” single-fibre response kernel, we are achieving an identifiable model to describe the extent, anisotropy and orientation of a fanning compartment. The model can be extended to multiple compartments, allowing estimation of fanning patterns that cross. We are also addressing the following important questions that have not been tackled by previous studies: a) Can we reliably estimate fannings and under which acquisition protocols? b) Can we dissociate fanning-induced dispersion from noise-induced uncertainty? c) How does such a model-based approach compare with non-parametric ODFs in the presence of fibre fanning? We present results on computer simulated data, representative of different fanning geometries. We also illustrate the potential of applying such an approach to high quality post-mortem macaque data, by presenting voxel-by-voxel maps of fibre dispersion.

2. Methods

2.1. The ball and rackets model

The ball and stick (BAS) model with one fibre population has been introduced by (Behrens et al., 2003) and decomposes the signal into a fully isotropic and a perfectly anisotropic compartment:

$$S_k = S_0\left[(1-f)\exp(-b_k d) + f\exp\left(-b_k d\left(\mathrm{g}_k^T\mathrm{v}\right)^2\right)\right] \quad (1)$$

with S_k, $k = 1{:}\ M$ the DW signal measured after the application of a diffusion-sensitising gradient with direction $\mathbf{g}_k$ and b value b_k, S_0 the signal without any diffusion weighting, d the mean diffusivity and $f \in [0, 1]$ the volume fraction of the anisotropic compartment with orientation $\mathbf{v} = [\sin\theta\cos\phi\ \sin\theta\sin\phi\ \cos\theta]^T$, $\theta \in [0,\pi]$ and $\phi \in [0,2\pi)$. If instead of a single fibre orientation $\mathbf{v}$, a continuous distribution of orientations $H(\theta, \phi)$ is assumed for the population, the model can be generalized to (Behrens et al., 2003):

$$S_k = S_0\left[(1-f)\exp(-b_k d) + f\int_0^{2\pi}\int_0^{\pi} H(\theta,\phi)\exp\left(-b_k d\left(\mathrm{g}_k^T\mathrm{v}\right)^2\right)\sin\theta\, d\theta\, d\phi\right] \quad (2)$$

The above model is a spherical convolution of function H with the single-fibre response kernel $\exp\left(-b_k d\left(\mathrm{g}_k^T\mathrm{v}\right)^2\right)$. The ball and stick model is a special case where H is a delta function (or a sum of deltas if multiple fibre populations are modelled), i.e. all axons in a population are assumed parallel to $\mathbf{v}$.

Estimation of H from the data is a deconvolution task. A popular method is to estimate it non-parametrically, in the space of some basis of functions (spherical harmonics for instance), where the deconvolution integrals become analytic (Tournier et al., 2004; Anderson, 2005). This has the disadvantage of estimating a spherical function that consequently needs further processing to extract relevant information, such as its local peaks. Also, the single-fibre response kernel is commonly assumed to be known. We are following a different - parametric - approach, where H is assumed to be a Bingham distribution, similar to (Kaden et al., 2007).

Let $H(\mathbf{v}) = F_B(\mathbf{v};\ \mathbf{B})$ be a Bingham distribution of $\mathbf{v}$ with parameter the 3×3 symmetric matrix $\mathbf{B}$. This distribution is axially symmetric, i.e. $F_B(\mathbf{v};\ \mathbf{B}) = F_B(-\mathbf{v};\ \mathbf{B})$ and its probability density is given by (Bingham, 1974; Mardia and Jupp, 2000):

$$F_B(\mathrm{v};\mathrm{B}) = \frac{1}{c_B}\exp\left(\mathrm{v}^T\mathbf{B}\mathrm{v}\right) \text{ with } c_B = 4\pi_1 F_1(1/2;3/2;\mathrm{B}) \quad (3)$$

and ${}_1F_1(\alpha;\ \beta;\ \mathbf{Z})$ is the confluent hypergeometric function of the first kind with a matrix argument. Then, substituting (3) into Equation (2), gives the following model (see Appendix A for derivation):

$$S_k = S_0\left[(1-f)\exp(-b_k d) + f\frac{{}_1F_1\left(1/2;3/2;\mathrm{B} - \mathbf{b_k}\mathbf{d}\mathrm{g_k}\mathrm{g_k^T}\right)}{{}_1F_1(1/2;3/2;\mathrm{B})}\right] \quad (4)$$

The Bingham matrix **B** is represented as $\mathbf{B} = \mathbf{R}^T\mathbf{B}_{diag}\mathbf{R}$, with **R** a rotation matrix and $\boldsymbol{B}_{diag}$ a diagonal matrix with two non-zero fanning eigenvalues $k_1 \geq k_2 > 0$. The rotation matrix consists of the spherical angles $\theta \in [0, \pi]$, $\boldsymbol{\phi} \in [0, 2\pi)$ and $\psi \in [0, \pi)$. The first two define the main *fibre orientation*, similar to the BAS model. Around this orientation fanning can occur depending on the eigenvalues of **B** and the angle ψ. The larger the eigenvalues, the less dispersion is modelled. The matrix **B** is parameterized as follows:

$\mathbf{B} = \mathbf{R}^T\mathbf{B}_{diag}\mathbf{R}$ and $\mathbf{R} = \mathbf{R}_\psi\mathbf{R}_\theta\mathbf{R}_{\boldsymbol{\phi}}$ with

$$\mathrm{R}_\psi = \begin{bmatrix} \cos(\psi) & \sin(\psi) & 0 \\ -\sin(\psi) & \cos(\psi) & 0 \\ 0 & 0 & 1 \end{bmatrix}, \mathrm{R}_\theta = \begin{bmatrix} \cos(\theta) & 0 & -\sin(\theta) \\ 0 & 1 & 0 \\ \sin(\theta) & 0 & \cos(\theta) \end{bmatrix}, \mathrm{R}_\phi = \begin{bmatrix} \cos(\phi) & \sin(\phi) & 0 \\ -\sin(\phi) & \cos(\phi) & 0 \\ 0 & 0 & 1 \end{bmatrix}, \mathrm{B}_{diag} = -\begin{bmatrix} k_1 & 0 & 0 \\ 0 & k_2 & 0 \\ 0 & 0 & 0 \end{bmatrix}.$$

Anisotropic ($k_1 > k_2$) and isotropic ($k_1 = k_2$) fanning can be represented, as Bingham is an assymetric distribution. In the absence of any dispersion, $k_1, k_2 \rightarrow \infty$ and the model-predicted signal converges to the one predicted by the BAS model. Angle ψ is meaningful only in the case of anisotropic fanning. It defines the orientation along which the biggest fanning extent occurs, relative to the y axis, when the fanning pattern is rotated on the x-y plane. It degenerates for isotropic cases. Thus, in the case of anisotropic fanning, a *fanning orientation* can be defined, apart from the main fibre orientation.

Equation 4 can be generalized to *N* crossing fibre populations, each potentially exhibiting dispersion, resulting to the mixture ball and rackets model:

$$S_k = S_0\left[\left(1 - \sum_{n=1}^{N} f_n\right)\exp(-b_k d) + \sum_{i=n}^{N} f_n \frac{{}_1F_1\left(1/2;3/2;\mathrm{B}_n - b_k d \mathrm{g}_k \mathrm{g}_k^T\right)}{{}_1F_1(1/2;3/2;\mathrm{B}_n)}\right] \quad (5)$$

with $0 \leq f_n \leq 1$ and $\sum_{n=1}^{N} f_n \leq 1$. This model allows multiple crossing populations to be resolved in each voxel, each having different dispersion features. The unknown parameters for each fibre population are f_n, θ_n, $\boldsymbol{\phi}_n$, ψ_n, k_{1n} and k_{2n}, $n = 1{:}\ N$, while d and S_0 are common for all populations.

The ball and rackets model has the same form when a Watson distribution (Watson, 1965) is used to parameterize *H*. Watson is a special case of Bingham with $k_1 = k_2 = \kappa$. For such a symmetric fanning model, the Bingham matrix reduces to $\mathrm{B}_n = k\boldsymbol{\mu}_n\boldsymbol{\mu}_n^T$, with κ related to the isotropic fanning extent (the larger κ the smaller the dispersion) and $\boldsymbol{\mu}$ being the main fibre orientation around which fanning occurs.

We should point out that our model is a special case of the one derived in (Kaden et al., 2007). In their work, a single-fibre response kernel is derived using the diffusion tensor formalism and also different diffusivities are allowed in the isotropic and anisotropic compartments. This causes identifiability issues between the volume fractions and the individual diffusivity parameters, at least for single-shell DW-MRI data. To overcome those, they fix all diffusivity parameters to emprirically-derived values, common to all voxels, which is not necessary in our approach. They further use a different parametrization for the Bingham matrix using three eigenvalues. Knowing that the addition of any constant to the eigenvalues does not change the distribution (Mardia and Jupp, 2000), we set k_3 to zero to reduce the number of model parameters.

The Bingham distribution has been employed to represent a fanning geometry, where a continuum of fibre orientations spread around a main orientation. However, a similar pattern of orientation dispersion can be anticipated for a bending geometry (Nedjati-Gilani and Alexander, 2009). Therefore, the ball and rackets model cannot differentiate between (within-voxel) fanning and bending patterns.

2.2. Implementation

In order to evaluate Equation (5), an approximation of the confluent hypergeometric function is needed. We used the theorem that for a $p \times p$ symmetric matrix $\mathbf{Z}$, ${}_1F_1(1/2; 3/2; \mathbf{Z}) = {}_1F_1(1/2; 3/2; \mathbf{Z}_{eig})$ with $\mathbf{Z}_{eig}$ a diagonal matrix with the eigenvalues of $\mathbf{Z}$ (Mardia and Jupp, 2000). After eigen-decomposing $\mathbf{Z}$, the confluent hypergeometric function with a diagonal matrix argument was approximated. A few alternatives were tried (Butler and Wood, 2002; Kume and Wood, 2005) with the latter being employed, as it gave smaller relative errors compared to numerical integration results.

A non-linear optimization routine was used to obtain estimates for the model parameters by minimizing the sum of squared residuals. A trust region reflective algorithm with finite differentiation of the Jacobian, as implemented in Matlab (Matlab R2011a, The Mathworks, Natick, MA), was utilised. To preserve the inequality $k_1 \geq k_2$ during optimization, k_2 was transformed so that the ratio $w = k_1/k_2$ was included instead into the model and optimized. The ratio was constrained to be $w \geq 1$ and $k_1 \geq 4$ to avoid too high dispersions (more than 70° isotropic) that would confound with the ball compartment. Furthermore, the volume fractions were constrained, such that $\sum_{n=1}^{N} f_n \leq 1$, by transforming $f_n = \beta_n \left(1 - \sum_{j=1}^{n-1} f_j\right)$, for $n \geq 2$ and $0 \leq \beta_n \leq 1$.

A challenging issue is to provide good starting points for the unknown parameters, in order to avoid the algorithm getting trapped in local minima. Information from the simpler ball and stick model can be used for this purpose. For a certain dataset, the BAS model is fitted and the estimates of d, S_0, f_n, θ_n and ϕ_n are used as starting points for the respective parameters of the ball and rackets. To initialize the fanning angles in case of anisotropic fannings, we use the eigenvectors of the inverse Hessian of the BAS cost function.

The Hessian is the matrix of second partial derivatives of a function. Assuming that the model residuals follow a Normal distribution (reasonable assumption for MRI data (Gudbjartsson and Patz, 1995)), the inverse Hessian of the sum of squared residuals, evaluated at the minimum of the cost function, provides an estimate of the covariance matrix of the model parameters. The principal eigenvector $\mathbf{e}_1$ of the inverse Hessian will point to the direction along which parameters exhibit large standard error, i.e. can move without greatly affecting the cost function. In the presence of anisotropic fanning, the fibre orientation estimate of the BAS model is expected to have large error (or small slope) along the major fanning orientation rather than across, suggesting that $\mathbf{e}_1$ should point along the former. Therefore, for each BAS orientation estimate, we evaluated the 3×3 Hessian matrix of the cost function, with respect to the x, y and z Cartesian coordinates, using the BAS estimated parameter values. The principal eigenvector of the inverse Hessian was then used to give a starting point for the fanning angle, as explained in detail in Appendix B.

We can also use the eigenvalues of the inverse Hessian to predict starting points for the fanning parameters k_1 and k_2. Even if no direct mapping is obvious, as the eigenvalues depend on the noise level as well, this can be learned similar to (Seunarine et al., 2007). We chose however to initialize these parameters using some intermediate fanning values (k_1 = 20 and k_2 = 5) that worked well in most of the cases.

2.3. Simulations

To simulate fibre fanning, a three-dimensional subvoxel grid was utilised, as described in (Nedjati-Gilani and Alexander, 2009) and implemented in Camino (Cook et al., 2006). Briefly, the fanning geometry features were determined by the position of the grid relative to a reference point. The orientation of the anisotropic compartment at each subvoxel was given by the radial line connecting its centre to the reference point. The signal of each subvoxel was then simulated using the ball and stick model. All the signals from the grid were averaged to obtain the simulated DW signal from a fanning pattern. Fanning anisotropy was varied by changing the dimensional anisotropy of the grid. For each subvoxel, the volume fraction of the anisotropic compartment was set to $f = 0.6$, the diffusivity to $d = 0.0012$ mm^2/s and $S_0 = 100$. Zero-mean Gaussian noise was added in quadrature to simulate the Rician nature of the MRI signal (Gudbjartsson and Patz, 1995). The signal to noise ratio (SNR) in the simulations was defined as S_0/σ_{noise}.

Simulations were utilised to evaluate the ball and rackets model and assess the effect of acquisition parameters (SNR, number of DW directions, *b* value) on the estimability of the model. We also tested our approach as well as five non-parametric, ODF-based techniques on reconstructing features of representative fanning geometries.

2.4. Macaque data

A diffusion-weighted MRI dataset of a perfusion-fixed macaque brain was acquired using a 4.7T Brucker scanner, as described in (D'Arceuil et al., 2007). In short, scans were performed using a 3D multi-shot, spin-echo sequence (acquisition matrix 128×142 with in-plane resolution 430×430 μm^2, TE=33 ms, TR=350 ms). Seventeen non-DW images were acquired, while diffusion weighting was applied along 120 uniformly distributed directions with b=8000 s/mm^2. 128 slices were acquired with a thickness of 430 μm. Total imaging time was 27 hours.

The SNR was estimated using the two-ROI approach and the appropriate correction factors, as described in (Gudbjartsson and Patz, 1995; Dietrich et al., 2007). Signal was obtained from a ROI in the midbody of the corpus callosum, where main fibre orientations are left-right. The SNR for a single b=0 volume was 45.2. For the DW volumes perpendicular and parallel to the main fibre orientation, the SNR was 28.5 and 13.2, respectively. (For comparison, SNR values for a standard in-vivo dataset that we obtain from a 3T Siemens TIM Trio are on the order of 13 for a single b=0 s/mm^2, and 8.5 and 3 for the b=1000 s/mm^2 DW volumes).

The DTI model (Basser et al., 1994) was applied to the dataset and the mean diffusivity (MD) map was extracted. A white matter (WM) mask was then obtained by applying FSL's FAST toolbox (Smith et al., 2004) on the MD image, which exhibited great contrast between white and gray matter due to the post-mortem tissue nature and the high b-value employed. The ball and rackets model was applied to the dataset and semi-quantitative maps of fanning dispersion were obtained. Indicative computation times per voxel were 0.133 and 0.34 seconds for the model with one and two Binghams, respectively, on a 3GHz CPU.

3. Results

3.1. Simulations

3.1.1. Single Fibre Fannings—We first tested the ball and rackets against resolving single fibre fannings. The model was fitted by minimizing the sum of squared residuals, as described in Methods. Figure 1 shows the resolved fanning distribution for different fanning extents. The left column illustrates the subvoxel grid that was used to simulate the signal.

The obtained orientations within a voxel are grouped together and shown in the next column. For different SNR values, the average Bingham distribution estimated across 15 simulations is presented to demonstrate the reproducibility of the estimates. We can observe that the smaller the fanning extent, the more difficult it is to resolve, as the changes induced in the signal are smaller.

In Figure 2 the fanning extent is kept constant, but its anisotropy is varied. The correct fanning pattern is reasonably resolved for SNR as low as 30, but much higher accuracy is achieved at lower noise levels. A correct pattern is also predicted when no fanning is present, with a stick-like distribution being estimated (bottom row of Figure 2). Some overfitting occurs due to noise, but the estimated fanning extent is small, illustrating the angular resolution of the approach. In agreement to Figure 1 results, low SNR values (≤ 15) impose significant challenges to the estimation, with the results being inadequate.

For a more quantitative evaluation, the Jensen-Shannon (JS) divergence (Lin, 1991) of the noise-free F and the noise-contaminated $\hat{F}$ distribution was computed for each simulation. The JS divergence is a bounded, symmetrized and smoothed version of the Kullback-Leibler (KL) divergence and assesses the similarity of two distributions. It takes values in the [0,1] interval, with $JS = 0$ signifying that F and $\hat{F}$ are equal. The JS divergence was computed as $JS(F\|\hat{F}) = 1/2\ (KL(F\|(\hat{F}+F)/2) + KL(\hat{F}\|(\hat{F}+F)/2))$, with $KL(F\|Q) = \sum_{i=1}^{P} F(\mathrm{x}_i) \log \frac{F(\mathrm{x}_i)}{Q(\mathrm{x}_i)}$, the KL divergence of F and Q and the set of $\{\mathbf{x}_i, i = 1{:}\ P\}$ points obtained on the sphere from a fourfold tessellation of an icosahedron. For each simulated geometry, the mean and standard deviation of the JS divergence across 15 simulations is reported in Table 1. As expected, the mean and standard deviation of the JS divergence increases with noise in all cases. The mean divergence is significantly high for SNR=15 (increases from 2 to 7 times, compared to the SNR=30 values), and even higher for SNR=10, suggesting poor estimation of the underlying distribution. For the no fanning cases, the JS divergence values are relatively high at all noise levels, as small deviations from the delta-like noise-free distribution are heavily penalized. In general, more concentrated distributions are more difficult to estimate.

The simulations of Figures 1 and 2 illustrate the importance of high SNR in resolving fanning configurations. Noise levels that are considered adequate for estimating the main fibre orientations (SNR<30) seem not high enough for robustly estimating fanning patterns. Indeed, the main fibre orientation is correctly estimated in all cases.

To test the sensitivity of the model estimates on acquisition parameters, we performed a series of simulations, varying the SNR, the number of diffusion-sensitising directions, the *b* value and the ground truth fanning pattern. For these simulations the signal was generated using the ball and rackets model, in order to have some ground-truth parameter values for comparing against. Representative results for an anisotropic fanning are shown in Figure 3. The ground truth ratio of the Bingham eigenvalues was fixed and the dispersion along both major and minor axes was varied for these simulations. Dispersion angle estimates (averaged across 15 realizations in each case) are shown along the main fanning orientation (major axis) and its normal orientation (minor axis) as well. The error in the estimated fanning orientation is also presented. Figure 3 presents only results obtained with 120 DW directions. Results with different number of directions are provided as supplementary material (Figures S1-S2). In general, a correct anisotropic pattern is resolved for SNR≥ 30, with smaller dispersions being more difficult to resolve. An anisotropic pattern for instance that extends 10 and 5 degrees along the two fanning axes respectively, is difficult to estimate even at an SNR of 60 (see the large error in the fanning orientation estimate). Nevertheless,

for intermediate dispersions, the errors for SNR≥ 30, *b*=2000 and 240 directions are less than 3 degrees.

Similar results were obtained for isotropic fanning patterns (supplementary Figure S3). Due to noise, the estimated patterns were slightly anisotropic, with the dispersions along the two axes being different. This effect was more evident for small ground truth dispersions (<20 degrees) and for higher noise levels. For intermediate dispersions though, at SNR≥ 45, *b*=2000 and 240 directions, the difference in the dispersion along the two axes was less than 6 degrees.

In agreement to the previous findings, these simulations illustrate the need for relatively high SNR data to correctly estimate the underlying fanning geometries. Even if increasing the angular resolution and/or the *b* value of the acquisition reduces estimation errors, increasing the SNR seems more beneficial. For instance (as shown in Figures S1 and S3), doubling the SNR from 15 to 30 gives better estimates than increasing the number of directions by a factor of 4, from 60 to 240. Notice that in both examples, acquisition time is quadrupled. Furthermore, HARDI datasets used routinely to resolve fibre crossings in-vivo (*b*=1000, 60 directions, SNR<30), do not seem to preserve fanning information.

3.1.2. Noise-induced uncertainty or fibre fanning?—A common misconception is that fanning-induced dispersion and noise-induced orientation uncertainty are confounded and cannot be dissociated during estimation. Figure 2 shows that both isotropic and anisotropic fanning patterns can be estimated in the presence of noise. Furthermore, in the absence of any fanning, noise causes overfitting, but the patterns that are estimated have small dispersion extent and minimal reproducibility.

To illustrate how differently fanning and noise are depicted during estimation, we simulated an isotropic fanning pattern and fitted the ball and rackets model to estimate the fanning distribution. We also fitted the ball and stick model and estimated the noise-induced uncertainty of the fibre orientation using a Bayesian framework (Behrens et al., 2003). The top panel of Figure 4 illustrates samples drawn from the posterior distribution of the fibre orientation of the BAS model given the data, for various SNR values; i.e. orientation uncertainty is illustrated. At very low SNR, the samples overlap with the ground truth fanning distribution, giving the impression of representing fanning information. However, the distribution of orientation samples becomes tighter as noise levels decrease, regardless of the presence of any fanning. On the contrary, the ball and rackets model estimates, shown at the bottom panel, improve with higher SNR, predicting better the isotropic fanning extent.

This is to be expected, given that the question we ask when fitting the ball and stick model is “where on the unit sphere does the biggest signal attenuation occur”. The presence of fanning does not change the location of the biggest signal dip (unless the distribution of orientations is uniform), resulting to low orientational uncertainty, which of course increases with increasing noise. On the contrary, the ball and rackets model is sensitive not only to the signal extrema, but also to the signal shape around them.

Similar observations hold for increasing the number of directions (results not shown), which were kept constant in these simulations. Indeed, in the hypothetical scenario of infinite amount of data being available, uncertainty in the fibre orientation in the ball and stick model will approach zero, regardless of any underlying fanning pattern. Given the advances in MR physics (field strength, gradient strength, sequence acceleration, artifact reduction) (for instance (Moeller et al., 2010)), better datasets are becoming available in terms of both SNR and number of datapoints. Due to this improved data quality, collectively depicted by the direction of the arrow in Figure 4, the uncertainty in the estimates of current models will

be reduced and models that explicitly include complex geometries and contain more information, such as fanning features, will become more estimable.

3.1.3. Crossings of Fibre Fannings—We tested the ball and rackets model for resolving crossings of fanning populations. A mixture of two Bingham distributions was fitted to the simulated signal, obtained from various combinations of fanning patterns. Perpendicular crossings of populations with the same or different fanning anisotropy, extent and fanning orientation were simulated. An example of the estimated distributions is shown in Figure 5. Figure S4 illustrates the estimates for the same pattern and more DW directions, which improve accuracy. Other representative examples are shown in the supplementary Figures S5-S9. The same trend was observed for all the tested patterns. Apart from the SNR, the effect of the *b* value was also important in these simulations. The correct pattern was estimated in a reproducible manner only for high enough *b* values, at SNR levels of at least 30. Low *b* value signals, typically acquired in DWI, seem to impose significant challenges to the estimation.

3.1.4. Comparison with non-parametric approaches—The ability to resolve fanning patterns was compared against the information contained in the shape of various ODF types, obtained through non-parametric approaches. Four representative patterns (very anisotropic, anisotropic, isotropic fanning and no fanning) were used to simulate data. The ball and rackets model was fitted to each dataset. ODFs were reconstructed in five different ways: a) Using the Funk-Radon transform (FRT) of the signal (Tuch, 2004; Descoteaux et al., 2007), b) Using the FRT and Laplacian sharpening (Descoteaux et al., 2005), c) Through a constant solid angle (CSA) marginalization of the diffusion scatter pattern (Aganj et al., 2010), d) By spherical deconvolution of the signal (Tournier et al., 2004) and e) By estimating the persistent angular structure (PAS) of the diffusion scatter pattern (Jansons and Alexander, 2003). FSL's ODF estimation toolbox (Smith et al., 2004; Sotiropoulos et al., 2011) was utilized for the first three and the MRtrix package for spherical deconvolution (J-D Tournier, Brain Research Institute, Melbourne, Australia, http://www.brain.org.au/software/). All these approaches used spherical harmonics as a basis set. The PAS function was estimated using Camino (Cook et al., 2006). To avoid having to perform regularization on the ODFs that would change their shape, we first tested all methods in noise-free data.

Figure 6 illustrates large differences in the potential of the different methods to resolve fanning patterns. In the presence of anisotropic fannings, ODFs tend to have peaks with anisotropic shapes that indicate correctly the fanning orientation. However, the extent and anisotropy of this shape heavily depends on the reconstruction method. The fanning extent is heavily overestimated by all diffusion ODFs. Fibre ODFs interestingly recover the geometry of the fanning grid, but also overestimate the fanning extent. Similar observations hold for isotropic or no-fanning scenarios. The PAS function is by far the sharpest amongst the ODF approaches, but its shape does not directly capture the fanning extent. The estimates of the ball and rackets model overlap well with the ground truth fibre orientation distributions.

We should point out that in the ODF reconstructions, a spherical harmonic order of 12 was employed, meaning 91 coefficients were estimated. When a lower harmonic order was utilised and the number of coefficients was reduced, all dODFs and fODFs had much broader shapes. Furthermore, fODFs exhibited small magnitude peaks at the origin due to truncation artifacts (Tournier et al., 2004). These are evident in the plots as oscillatory patterns on the sphere. For the PAS functions, their shape was heavily dependent on the filtering parameter *r*, as this directly changes the deconvolution kernel. We used a value of $r = 1.55$, which was found optimal for these simulations. Small changes to it (i.e. 1.53 or 1.57) changed massively the shape and the broadness of the peak.

We further tested the sharpest approaches (SD fODFs and PAS) against noise. Spherical deconvolution is very sensitive to noise and fails to give meaningful results at such high harmonic orders. We therefore compared ball and rackets with fODFs obtained using constrained spherical deconvolution (CSD) (Tournier et al., 2007). As shown in Figure 7, CSD fODFs were robust to noise, but less sharp than their noise-free SD counterparts (Figure 6). Regarding PAS, the peak shape varied significantly depending on the value of the filtering parameter r. We fixed r to the value that was found optimal for the noise-free cases. In all simulated scenarios, the ball and rackets model provided estimates that were informative on the fanning extent and anisotropy.

3.2. Macaque Data

The ball and rackets model with one fibre compartment was fitted to the macaque brain dataset. The estimated fanning eigenvalues k_1 and k_2 were converted to dispersion angles corresponding to the 50% of the distribution along the major and minor fanning axes. Maps of the mean fanning (MF) extent were generated by plotting on a voxel-by-voxel basis the mean of these two angles, as shown in Figure 8. For better visualization, dispersion values are presented only in white matter, as the values in gray matter and CSF are not particularly meaningful; the anisotropic volume fraction in these regions is small and the fanning parameters degenerate.

Figure 8 also presents maps of the anisotropic volume fraction f_1. In general, estimated values for f_1 were higher when fitting the ball and rackets compared to estimates obtained from the ball and stick model. The mean (and standard deviation) of f_1 in white matter were 0.3624 (0.1538) for the former and 0.2305 (0.1348) for the latter, suggesting that in the first case a higher fraction of the signal was explained by the anisotropic compartment.

Many interesting patterns can be observed in the presented maps. Low fanning indices are generally present in the body of the corpus callosum (CC) (Figure 8a and 8c-d). A spatial pattern of low-high-low values is observed bilaterally, as we move from medial to lateral callosal regions (Figure 8a and 8c). This can be indicative of fibre bending that is expected in the CC body, just before callosal projections enter the centrum semiovale (as pointed out in Methods, the model cannot differentiate between dispersion caused by fanning or bending). Furthermore, despite the low dispersion values overall, slightly different dispersion patterns in the splenium, genu and midbody are suggested by the midsaggital view of Figure 8d. The splenium and genu seem more coherent than the midbody, where MF values increase. This agrees with findings from (Zhang et al., 2011) and as suggested in (Barazany et al., 2009) may be due to differences in axon diameters in these regions. Larger axons in the midbody may not facilitate as coherent and organized packing as in the splenium and the genu, where axons have smaller diameters.

Higher dispersion values are predicted in the internal capsule (Figure 8b and 8e)), especially in its posterior limb. An interesting pattern is also observed in the vicinity of the most cortical gyri. Two representative examples are shown in Figure 8f. As white matter approaches the gyral walls, fanning indices gradually increase, having low values midway between the two adjacent walls. This pattern suggests coherent bundles that stem from/arrive to the gyri and fan in a roughly uniform way towards the gyral walls.

A few more regions, where minimum fanning is expected and low MF values are estimated, are illustrated. Low fanning values for parts of the optic radiation are shown in Figure 8a, indicated by the white arrow. Similarly for part of the fornix (Figure 8d) and the anterior commissure (Figure 8g).

On a more pictorial representation, Figure 9 illustrates estimated Bingham distributions on spherical plots for different white matter regions. The fanning distributions for a group of voxels in the body of the corpus callosum are plotted in Figure 9a and 9b, corresponding to a midsagittal and a more lateral slice respectively. The fanning extent is minimal in the medial region, but it is considerably larger for the lateral slice, where the fanning distribution potentially reflects bending of the callosal fibres. Interestingly, the orientation of the major fanning axis deviates more from the superior-inferior axis as we move towards the splenium of the corpus callosum. This agrees with the anticipated route of callosal fibres; towards superior regions in the midbody and towards posterior regions in the splenium, supporting the argument that fibre bending is depicted.

Similar plots are presented for a group of voxels in the internal capsule (Figure 9c). Anisotropic distributions are predicted with the main fanning orientation being mostly aligned with the anterior-posterior axis. We should point out that very anisotropic distributions potentially reflect crossings of underlying coherent fibre populations (i.e. with a “stick” profile) or populations with similar fanning patterns. Examples of estimated distributions when fitting one or two fibre compartments are presented in Figure 10. The crossing between the corticospinal tract and the transverse pontine fibres is depicted in panel 10a. The former exhibits a fanning pattern with a large extent and anterior-posterior anisotropy. The latter has a coherent profile with no fanning, but a larger volume fraction so that it dominates the signal contribution. Therefore, when fitting a one Bingham model the estimated distribution has a major orientation close to the medio-lateral orientation of the pontine fibres and similar fanning features.

Figure 10b on the other hand illustrates a crossing of two similar fanning patterns at the centrum semiovale, between callosal and longitudinal fibres. When fitting one fibre compartment, the estimated distribution is anisotropic and has an extent that covers both fanning compartments. Clearly, model selection is necessary to correctly estimate individual fanning patterns and avoid overfitting.

Figure 11 illustrates the main fibre orientations estimated from the ball and rackets model at a centrum semiovale region. Estimates from a model with one and two anisotropic compartments are shown. To ease visualization, secondary fibres are presented only in voxels included in the white matter mask. We can observe that the orientation estimates are spatially smooth and agree with our anatomical knowledge in this crossing region. As before, model selection is needed to choose in each voxel between the one and two-Bingham model estimates. We are currently investigating model selection strategies, to help decide between similar situations in real data.

4. Discussion and Conclusions

We have presented and evaluated a model for directly estimating fibre orientation dispersion, driven by underlying complex geometries, such as within-voxel fibre fanning and bending. Ball and rackets is a multi-compartment model that captures both (isotropic) partial volume and (anisotropic) fibre populations. The model assumes that a fibre population can be represented as a continuous Bingham distribution of orientations, centred around a main orientation. Assuming a discrete number of populations, without exchange between them, the model can be extended to a a finite mixture of Bingham distributions. Dispersion features, represented by parameters of these distributions, can be explicitly estimated from diffusion-weighted MRI. To illustrate the potential of the approach, we have presented whole-brain spatial maps of the dispersion extent using high quality, post-mortem macaque data and the estimated distributions in different white matter regions.

We have also used extensive computer simulations to address for the first time the following questions: 1) Under which acquisition protocols, such a dispersion model can be robustly fitted? 2) Can we dissociate orientation dispersion that is present due to underlying tissue structure from noise-induced dispersion? 3) How does a model-based approach compare with non-parametric, ODF-based techniques in extracting dispersion-related information?

We have found that the value of the signal to noise ratio has a profound effect on the estimation of orientation dispersion (Figures 2, 3 and S1-S3). SNR values that have been considered high enough for estimating crossing fibres ($10 \leq SNR \leq 30$) seem not adequate for robustly resolving fanning patterns. This is because dispersion features affect the shape of the signal, rather than its local extrema; the former being much more sensitive to noise artifacts. In the presence of multiple fanning geometries that cross, a high *b* value is also necessary to achieve angular contrast enough to dissociate the dispersion features of the different populations (Figure 5). Furthermore, the smaller the ground truth dispersion and the more isotropic, the more difficult it is to correctly estimate. In the first case, this is due to the small signal changes induced compared to the signal obtained from a perfectly coherent pattern. In the second case, perfectly isotropic profiles cannot be resolved from noisy measurements, for a similar reason that perfectly isotropic tensors appear slightly anisotropic in DTI (Pierpaoli and Basser, 1996).

We illustrated and discussed the difference between fanning and noise-induced orientation dispersion. To estimate the latter, we applied Bayesian inference to the ball and stick model, which does not explicitly represent fanning geometries. Using a toy example, we showed that modelled biophysical dispersion is not confounded by noise-induced uncertainty. The fibre orientation uncertainty always reduced as SNR or number of datapoints increased, regardless of the underlying tissue geometry. Interestingly though, in the presence of fanning, the ball and stick model provided useful information through the inverse Hessian of the cost function, which we utilized for initializing the non-linear fitting routine of the ball and rackets.

We have further explored the ability of various non-parametric approaches, commonly used to resolve crossing fibres, to reflect fanning geometries and dispersion features in their shape. Diffusion ODFs, fibre ODFs and the PAS function were reconstructed on representative fanning geometries (Figure 6). In the presence of fanning, all functions exhibited broad peak shapes, which were also anisotropic in the presence of anisotropic fanning, in agreement with (Seunarine and Alexander, 2009). However, peak shapes were massively different across different methods, making the mapping of peak shape characteristics to dispersion features unobvious. The situation can be complicated even more by regularization approaches that are typically employed to reduce noise artifacts. Commonly used regularization techniques preserve the location of ODF local maxima, however interfere with the shape of the function (Figure 7). Therefore, even if the underlying tissue geometry affects the ODF shape, the extraction of relevant information might be challenging and still require a parametric post-processing step. The ball and rackets model, on the other hand, preserved the relative shape of the estimated distributions in the presence of noise and offered a direct mapping of parameters to geometrical features.

For the computer simulations, we utilized a subvoxel grid to mimic various fanning geometries. The simulated signal was the average of many elementary signal components, obtained at the grid points, using the ball and stick model. Given that the single-fibre response in the ball and rackets model is motivated by a stick compartment, we expect that deviations from this behaviour will lead to over-estimation of dispersion. However, this is a common problem for all deconvolution approaches, where a single-fibre response kernel needs to be defined (Tournier et al., 2004; Anderson, 2005; Kaden et al., 2007). Commonly,

a kernel is pre-specified for all voxels in the brain, but we allowed greater flexibility by treating the diffusivity *d* as a model parameter and permitting variations to the kernel across voxels.

We should point out that the ball and rackets model, in its current form, is intended for single-shell diffusion data. The single fibre response kernel is monoexponential and cannot accurately capture the signal behaviour at multiple shells. The kernel should be modified for such a purpose. Multi-shell data will allow dissociation of diffusivities between different compartments (for instance a different diffusion coefficient can be used in the model for the isotropic and anisotropic compartments) and better estimation of the model parameters. However, not all multi-shell kernels will yield a closed form for the spherical deconvolution expression (Eq. 2). An example is presented in (Zhang et al., 2011), where the single fibre response kernel models microstructural properties of the tissue, but the less complex Watson distribution has to be utilized to achieve a closed form expression.

To explore the potential of the proposed parametric approach, we used post-mortem macaque data that were of high quality and angular resolution. By fitting the ball and rackets, we obtained spatial maps of dispersion extent that revealed fanning and bending geometries (Figure 8). However, the high SNR and angular resolution of the employed dataset raises the question of whether the presented method is applicable in-vivo. Advances in the MR physics and new acceleration methods, such as multiband EPI (Moeller et al., 2010), have already allowed significant reductions in acquisition time. In the near future, this will permit multiple repeats and directions to be acquired during a single scanning session. In fact, projects such as the Human Connectome Project (http://humanconnectome.org/) aim to build large databases of such high quality data and make them available to the community. We hope that the ball and rackets model will be applicable in-vivo in the very near future.

We illustrated, both in simulations and real data, the potential of estimating two fanning compartments that cross. In the case of crossing fibres with no fanning, the model performs well (Figure S9), given that the correct number of compartments are included in the model. There is a model selection issue, which we do not explore here and will be the aim of a future study. We are currently exploring Bayesian inference approaches that utilize shrinkage priors on the fanning parameters and the number of compartments to address this issue (Behrens et al., 2007). A Bayesian framework will also allow the estimation of the uncertainty in the dispersion distributions, similar to the estimation of uncertainty in the fibre orientation that is commonly used in probabilistic tractography (Parker and Alexander, 2003; Behrens et al., 2003).

4.1. Implications for tractography

We anticipate incorporation of dispersion information into tractography methods to be important for three main reasons: a) modeling a fanning pattern by simply using the mean orientation (e.g. ODF local maxima) and ignoring the spreading is likely to induce false negatives; b) accounting for these complex geometries at the voxel level will allow to distinguish between fibre dispersion and noise-induced uncertainty (Figure 4 and (Kaden et al., 2007)); and c) the estimated distributions can be utilized in spatial models to infer fanning polarity, which may increase both sensitivity and secificty in tractography (Jbabdi and Johansen-Berg, 2011). However, developing tractography algorithms that benefit from these advances is not straightforward.

In its simplest form, utilization of dispersion information in tractography can be performed in an hierarchical way, as suggested by (Behrens and Jbabdi, 2009). This requires a framework to assess the uncertainty of the estimated distributions. N orientation samples

from the dispersion distributions can then be drawn to perform streamline probabilistic tractography, as usual. This can be repeated M times, by drawing new dispersion distributions from the underlying uncertainty distributions. The process can give a reproducibility measure for the path connection probabilities estimated from probabilistic tractography. Current methods (e.g. fODFs) can be used for this purpose, but as shown in Figures 6-7, the ball and rackets estimates may be more specific, reducing false positives.

Another useful application would be the incorporation of the local dispersion models in spatial geometrical models for inferring fanning polarity. A main limitation of the ball and rackets model is its inability to characterize polarity. The estimated distributions are by construction axially symmetric and are sensitive to the set of orientations being present within a voxel rather than their exact spatial arrangement, as shown in Figure 1. For the same reason, fanning and bending cannot be differentiated. This limitation stems from the symmetric nature of diffusion data and cannot be tackled on a single voxel basis (Jbabdi and Johansen-Berg, 2011). To estimate asymmetric distributions, asymmetric data need to be available and this can achieved only by pooling information across space. Assessing fanning asymmetry and polarity is necessary for increasing tractography specificity. Otherwise, undesired propagation of curves towards the wrong direction, driven by the symmetricity of dispersion distributions, may occur. Early attempts for incorporating spatial information to distinguish different spatial patterns have been presented by (Savadjiev et al., 2008), that use only the main fibre orientation estimates in each voxel to dissociate bending from crossing. We anticipate that incorporation of dispersion information will be beneficial within similar frameworks.

Supplementary Material

Refer to Web version on PubMed Central for supplementary material.

Acknowledgments

We would like to thank Dr Helen D'Arceuil and Dr Alex de Crespigny for providing us with the macaque dataset. Furthermore, Dr Donald Tournier and Dr Kiran Seunarine for assisting us with the Mrtrix spherical deconvolution and the Camino PASMRI implementations, respectively. We would like to acknowledge funding from the the EU CONNECT project, the Wellcome Trust (WT088312AIA), the UK Medical Research Council(G0800578) and the Human Connectome Project (1U54MH091657-01) from the 16 NIH Institutes and Centers that support the NIH Blueprint for Neuroscience Research. The project “CONNECT” acknowledges the financial support of the Future and Emerging Technologies (FET) programme within the Seventh Framework Programme for Research of the European Commission, under FET-Open grant number: 238292.

Appendix A. Derivation of the ball and rackets model

Substituting (3) into Equation (2):

$$S_k = S_0\left[(1-f)\exp(-b_k d) + f\int_{S^2}\frac{1}{c_B}\exp\left(\mathrm{v}^T\mathbf{B}\mathrm{v}\right)\exp\left(-b_k d\left(\mathrm{g}_k^T\mathrm{v}\right)^2\right)d\mathrm{v}\right]$$
$$= S_0\left[(1-f)\exp(-b_k d) + \frac{f}{c_B}\int_{S^2}\exp\left(\mathrm{v}^T\mathbf{B}\mathrm{v} - \mathbf{b_k d}\left(\mathrm{g}_{\mathbf{k}}^{\mathbf{T}}\mathrm{v}\right)^{\mathbf{2}}\right)d\mathrm{v}\right]$$

If we rewrite $\left(\mathrm{g}_k^T\mathrm{v}\right)^2 = \left(\mathrm{v}^T\mathrm{g}_k\right)^2 = \left(\mathrm{v}^T\mathrm{g}_k\right)\left(\mathrm{g}_k^T\mathrm{v}\right) = \mathrm{v}^T\mathbf{g}_k\mathrm{g}_k^T\mathrm{v}$, then this a quadratic form in the elements of **v**, similarly to $\mathbf{v}^T\mathbf{B}\mathbf{v}$. We can therefore factor out the elements of **v** and get:

$$
\begin{aligned}
S_k &= S_0\left[(1-f)\exp(-b_k d) + \frac{f}{c_{\mathrm{B}}}\int_{S^2}\exp\left(\mathrm{v}^T\left(\mathrm{B}-\mathbf{b_k d g_k g_k^T}\right)\mathrm{v}\right)d\mathrm{v}\right] \\
&= S_0\left[(1-f)\exp(-b_k d) + \frac{f}{c_{\mathrm{B}}}\int_{S^2}\exp\left(\mathrm{v}^T\mathbf{Q}\mathbf{v}\right)d\mathrm{v}\right] \\
&= S_0\left[(1-f)\exp(-b_k d) + f\frac{c_Q}{c_B}\right] \\
&= S_0\left[(1-f)\exp(-b_k d) + f\frac{{}_1F_1\left(1/2;3/2;\mathrm{B}-\mathbf{b_k d g_k g_k^T}\right)}{{}_1F_1\left(1/2;3/2;\mathrm{B}\right)}\right]
\end{aligned}
$$

The equality $\int_{S^2}\exp\left(\mathrm{v}^T\mathbf{Q}\mathbf{v}\right)d\mathrm{v}=\mathbf{c}_{\mathrm{Q}}\int_{\mathbf{S^2}}\mathbf{F}_{\mathbf{B}}\left(\mathrm{v};\mathrm{Q}\right)\mathbf{d}\mathrm{v}=\mathbf{c}_{\mathrm{Q}}$ has been used above.

Appendix B. Predicting anisotropic fanning orientations from the ball and stick model

For each orientation estimate **u** of the ball and stick model, we evaluate the 3×3 Hessian matrix of the cost function, with respect to the x, y and z Cartesian coordinates, using the model estimated parameter values. We then project the inverse Hessian to the plane perpendicular to **u**, as fanning will always occur perpendicular to the fibre orientation. If anisotropic fanning occurs about **u**, the principal eigenvector of the projected inverse Hessian will point along the main fanning orientation.

Let (**x, y, z**) be a Cartesian coordinate system and **u** a column vector with coordinates in this system. Then:

- Define **v** and **w** orthogonal to **u**, such that (**u, v, w**) is an orthonormal coordinate system.
- Define the transformation matrix **A**=[**u** | **v** | **w**]. Then, $\mathbf{A^{-1}} = \mathbf{A}^T$ transforms coordinates from (**x, y, z**) to the local (**u, v, w**) system.
- Let P= $[[0\ 0\ 0]^T \mid [0\ 1\ 0]^T \mid [0\ 0\ 1]^T]$ be a projection matrix. The projection of the inverse Hessian on the **v**-**w** plane will then be $\mathbf{C} = \mathbf{Q}\mathbf{H}^{-1}\mathbf{Q}^T$, with $\mathbf{Q} = \mathbf{P}\mathbf{A}^T$.
- The principal eigenvector $\mathbf{e}_1$ of **C** will be on the (**u, v, w**) coordinate system. The vector $\mathbf{A}\mathbf{e}_1$ will be in the original (**x, y, z**) system and provide an estimate for the fanning orientation, as shown in Figure 12a.

The Hessian used above is calculated with respect to the x, y and z Cartesian coordinates of vector **u**:

$$
\mathrm{H}=\begin{bmatrix}
\frac{\partial^2 E}{\partial x^2} & \frac{\partial^2 E}{\partial x \partial y} & \frac{\partial^2 E}{\partial x \partial z} \\
\frac{\partial^2 E}{\partial x \partial y} & \frac{\partial^2 E}{\partial y^2} & \frac{\partial^2 E}{\partial y \partial z} \\
\frac{\partial^2 E}{\partial x \partial z} & \frac{\partial^2 E}{\partial y \partial z} & \frac{\partial^2 E}{\partial z^2}
\end{bmatrix},
$$

with E being the sum of squared model residuals. **H** is evaluated at the ball and stick estimated parameter values.

Figure 12 shows how this method can predict the fanning orientation, when one or more fanning populations are simulated. We use these predictions in order to initialize parameters ψ_n.

References

Aganj I, Lenglet C, Sapiro G, Yacoub E, Ugurbil K, Harel N. Reconstruction of the orientation distribution function in single and multiple shell q-ball imaging within constant solid angle. Magnetic Resonance in Medicine. 2010; 64(2):554–566. [PubMed: 20535807]

Alexander DC. Maximum entropy spherical deconvolution for diffusion MRI. Information Processing in Medical Imaging (IPMI). 2005; 19:76–87.

Anderson AW. Measurement of fiber orientation distributions using high angular resolution diffusion imaging. Magnetic Resonance in Medicine. 2005; 54(5):1194–206. [PubMed: 16161109]

Assaf Y, Basser PJ. Composite hindered and restricted model of diffusion (CHARMED) MR imaging of the human brain. Neuroimage. 2005; 27(1):48–58. [PubMed: 15979342]

Assemlal, HE.; Campbell, J.; Pike, B.; Siddiqi, K. Apparent intravoxel fibre population dispersion (FPD) using spherical harmonics. In: Fichtinger, G.; Martel, A.; Peters, T., editors. MICCAI Proceedings. 2011. p. 157-165.

Barazany D, Basser PJ, Assaf Y. In-vivo measurement of the axon diameter distribution in the corpus callosum of a rat brain. Brain. 2009; 132:1210–1220. [PubMed: 19403788]

Basser PJ, Mattiello J, LeBihan D. Estimation of the effective self-diffusion tensor from the NMR spin echo. Journal of Magnetic Resonance Series b. 1994; 103:247–54. [PubMed: 8019776]

Basser PJ, Pajevic S, Pierpaoli C, Duda J, Aldroubi A. In vivo fiber tractography using DT-MRI data. Magnetic Resonance in Medicine. 2000; 44(4):625–32. [PubMed: 11025519]

Behrens TE, Berg HJ, Jbabdi S, Rushworth MF, Woolrich MW. Probabilistic diffusion tractography with multiple fibre orientations: What can we gain? Neuroimage. 2007; 34(1):144–55. [PubMed: 17070705]

Behrens TE, Woolrich MW, Jenkinson M, Johansen-Berg H, Nunes RG, Clare S, Matthews PM, Brady JM, Smith SM. Characterization and propagation of uncertainty in diffusion-weighted MR imaging. Magnetic Resonance in Medicine. 2003; 50(5):1077–88. [PubMed: 14587019]

Behrens, TEJ.; Jbabdi, S. MR diffusion tractography. In: Johansen-Berg, H.; Behrens, T., editors. Diffusion MRI: From quantitative measurement to in vivo neuroanatomy. Elsevier; 2009. p. 333-352.

Bingham C. An antipodally symmetric distribution on the sphere. Annals of Statistics. 1974; 2(6): 1201–1225.

Butler RW, Wood ATA. Laplace approximations for hypergeometric functions with matrix arument. The Annals of Statistics. 2002; 30(4):1155–1177.

Catani M, Howard RJ, Pajevic S, Jones DK. Virtual in vivo interactive dissection of white matter fasciculi in the human brain. Neuroimage. 2002; 17(1):77–94. [PubMed: 12482069]

Conturo TE, Lori NF, Cull TS, Akbudak E, Snyder AZ, Shimony JS, McKinstry RC, Burton H, Raichle ME. Tracking neuronal fiber pathways in the living human brain. Proceedings of the National Academy of Sciences. 1999; 96(18):10422–7.

Cook, P.; Bai, Y.; Nedjati-Gilani, S.; Seunarine, KK.; Hall, MG.; Parker, GJ.; Alexander, DC. Camino: Open-source diffusion-MRI reconstruction and processing. Proceedings of the International Society for Magnetic Resonance in Medicine (ISMRM) Meeting; Seattle, USA. 2006. p. 2759

D'Arceuil H, Westmoreland S, de Crespigny AJ. An approach to high resolution diffusion tensor imaging in fixed primate brain. NeuroImage. 2007; 35:553–565. [PubMed: 17292630]

Dell'Acqua F, Rizzo G, Scifo P, Clarke RA, Scotti G, Fazio F. A model-based deconvolution approach to solve fiber crossing in diffusion-weighted mr imaging. IEEE Transactions on Biomedical Engineering. 2007; 54(3):462–472. [PubMed: 17355058]

Descoteaux M, Angelino E, Fitzgibbons S, Deriche R. A linear and regularized odf estimation algorithm to recover multiple fibers in q-ball imaging. Tech rep, INRIA Research Report 5768. 2005

Descoteaux M, Angelino E, Fitzgibbons S, Deriche R. Regularized, fast, and robust analytical Q-ball imaging. Magnetic Resonance in Medicine. 2007; 58(3):497–510. [PubMed: 17763358]

Descoteaux M, Deriche R, Knosche TR, Anwander A. Deterministic and probabilistic tractography based on complex fibre orientation distributions. IEEE Transactions on Medical Imaging. 2009; 28(2):269–86. [PubMed: 19188114]

Dietrich O, Raya JG, Reeder SB, Reiser MF, Schoenberg SO. Measurement of signal-to-noise ratios in MR images: influence of multichannel coils, parallel imaging, and reconstruction filters. Journal of Magnetic Resonance Imaging. 2007; 26(2):375–385. [PubMed: 17622966]

Gudbjartsson H, Patz S. The Rician distribution of noisy MRI data. Magnetic Resonance in Medicine. 1995; 34(6):910–4. [PubMed: 8598820]

Jansons KM, Alexander DC. Persistent angular structure: new insights from diffusion magnetic resonance imaging data. Inverse Problems. 2003; 19:1031–1046.

Jbabdi S, Johansen-Berg H. Tractography: Where do we go from here? Brain Connectivity. 2011 in press.

Kaden E, Knosche TR, Anwander A. Parametric spherical deconvolution: inferring anatomical connectivity using diffusion MR imaging. Neuroimage. 2007; 37(2):474–488. [PubMed: 17596967]

King MD, Gadian DG, Clark CA. A random effects modelling approach to the crossing-fibre problem in tractography. NeuroImage. 2009; 44:753–768. [PubMed: 19007890]

Kreher BW, Schneider JF, Mader I, Martin E, Hennig J, Il'yasov KA. Multitensor approach for analysis and tracking of complex fiber configurations. Magnetic Resonance in Medicine. 2005; 54:1216–25. [PubMed: 16200554]

Kume A, Wood ATA. Saddlepoint approximations for the Bingham and Fisher-Bingham normalising constants. Biometrika. 2005; 92(2):465–476.

Lazar M, Jensen JH, Xuan L, Helpern JA. Estimation of the orientation distribution function from diffusional kurtosis imaging. Magnetic Resonance in Medicine. Oct; 2008 60(4):774–781. [PubMed: 18816827]

Le Bihan D, Breton E, Lallemand D, Grenier P, Cabanis E, Laval-Jeantet M. MR imaging of intravoxel incoherent motions: application to diffusion and perfusion in neurologic disorders. Radiology. Nov; 1986 161(2):401–407. [PubMed: 3763909]

Leow AD, Zhu S, Zhan L, McMahon K, de Zubicaray GI, Meredith M, Wright MJ, Toga AW, Thompson PM. The tensor distribution function. Magnetic Resonance in Medicine. 2009; 61(1): 205–214. [PubMed: 19097208]

Lin J. Divergence measures based on the Shannon entropy. IEEE Transactions on Information Theory. 1991; 37(1):145–151.

Mardia, KV.; Jupp, PE. Directional Statistics. John Wiley & Sons; 2000. Distributions on spheres; p. 159-192.

Moeller S, Yacoub E, Olman CA, Auerbach E, J S, Harel N, Ugurbil K. Multiband multislice ge-epi at 7 tesla, with 16-fold acceleration using partial parallel imaging with application to high spatial and temporal whole-brain fmri. Magnetic Resonance in Medicine. 2010; 63(5):1144–1153. [PubMed: 20432285]

Mori S, Crain BJ, Chacko VP, van Zijl PC. Three-dimensional tracking of axonal projections in the brain by magnetic resonance imaging. Annals of Neurology. 1999; 45:265–9. [PubMed: 9989633]

Nedjati-Gilani, S.; Alexander, DC. Models for fanning and bending sub-voxel structures in diffusion MRI. Proceedings of the DMFC MICCAI 2009 Workshop; London, UK. 2009.

Ozarslan E, Shepherd TM, Vemuri BC, Blackband SJ, Mareci TH. Resolution of complex tissue microarchitecture using the diffusion orientation transform (DOT). Neuroimage. 2006; 31:1086–103. [PubMed: 16546404]

Parker GJ, Alexander DC. Probabilistic Monte Carlo based mapping of cerebral connections utilising whole-brain crossing fibre information. Information Processing in Medical Imaging (IPMI). 2003; 18:684–95.

Patel V, Shi Y, Thompson PM, Toga AW. Mesh-based spherical deconvolution: A flexible approach to reconstruction of non-negative fiber orientation distributions. NeuroImage. 2010; 51(3):1071–1081. [PubMed: 20206705]

Peled S, Friman O, Jolesz F, Westin CF. Geometrically constrained two-tensor model for crossing tracts in DWI. Magnetic Resonance Imaging. 2006; 24:1263–70. [PubMed: 17071347]

Pierpaoli C, Basser PJ. Toward a quantitative assessment of diffusion anisotropy. Magnetic Resonance in Medicine. 1996; 36:893–906. [PubMed: 8946355]

Pierpaoli C, Jezzard P, Basser PJ, Barnett A, Di Chiro G. Diffusion tensor MR imaging of the human brain. Radiology. 1996; 201:637–48. [PubMed: 8939209]

Savadjiev P, Campbell JSW, Descoteaux M, Deriche R, Pike GB, Siddiqi K. Labeling of ambiguous subvoxel fibre bundle configurations in high angular resolution diffusion MRI. Neuroimage. 2008; 41(1):58–68. [PubMed: 18367409]

Savadjiev P, Kindlmann GL, Bouix S, Shenton ME, Westin CF. Local white matter geometry from diffusion tensor gradients. Neuroimage. 2010; 49:3175–3186. [PubMed: 19896542]

Seunarine, KK.; Alexander, DC. Multiple fibers: Beyond the diffusion tensor. In: Johansen-Berg, H.; Behrens, T., editors. Diffusion MRI: From quantitative measurement to in vivo neuroanatomy. Elsevier; 2009. p. 55-72.

Seunarine KK, Cook PA, Hall MG, Embleton KV, Parker GJM, Alexander DC. Exploiting peak anisotropy for tracking through complex structures. Proceedings of the IEEE International Conference on Computer Vision Workshop on MMBIA. 2007

Smith SM, Jenkinson M, Woolrich MW, Beckmann CF, Behrens TE, Johansen-Berg H, Bannister PR, De Luca M, Drobnjak I, Flitney DE, Niazy RK, Saunders J, Vickers J, Zhang Y, De Stefano N, Brady JM, Matthews PM. Advances in functional and structural MR image analysis and implementation as FSL. Neuroimage. 2004; 23 1:S208–19. [PubMed: 15501092]

Sotiropoulos, SN.; Aganj, I.; Jbabdi, S.; Sapiro, G.; Lenglet, C.; Behrens, TEJ. Inference on constant solid angle orientation distribution functions from diffusion-weighted mri. OHBM Annual Meeting; Quebec, Canada. June. 2011

Sotiropoulos SN, Bai L, Morgan PS, Auer DP, Constantinescu CS, Tench CR. A regularized two-tensor model fit to low angular resolution diffusion images using basis directions. Journal of Magnetic Resonance Imaging. 2008; 28:199–209. [PubMed: 18581343]

Tournier JD, Calamante F, Connelly A. Robust determination of the fibre orientation distribution in diffusion MRI: non-negativity constrained super-resolved spherical deconvolution. Neuroimage. 2007; 35:1459–72. [PubMed: 17379540]

Tournier JD, Calamante F, Gadian DG, Connelly A. Direct estimation of the fiber orientation density function from diffusion-weighted MRI data using spherical deconvolution. Neuroimage. 2004; 23:1176–85. [PubMed: 15528117]

Tuch DS. Q-ball imaging. Magnetic Resonance in Medicine. 2004; 52:1358–72. [PubMed: 15562495]

Tuch DS, Reese TG, Wiegell MR, Makris N, Belliveau JW, Wedeen VJ. High angular resolution diffusion imaging reveals intravoxel white matter fiber heterogeneity. Magnetic Resonance in Medicine. 2002; 48:577–82. [PubMed: 12353272]

Watson GS. Equatorial distributions on a sphere. Biometrika. 1965; 52(1-2):193–201.

Wedeen VJ, Hagmann P, Tseng WY, Reese TG, Weisskoff RM. Mapping complex tissue architecture with diffusion spectrum magnetic resonance imaging. Magnetic Resonance in Medicine. 2005; 54:1377–86. [PubMed: 16247738]

Yeh FC, Wedeen VJ, Tseng WY. Estimation of fibre orientation and spin density distribution by diffusion deconvolution. Neuroimage. 2011; 55(3):1054–1062. [PubMed: 21232611]

Yeh FC, Wedeen VJ, Tseng WYI. Generalized q-sampling imaging. IEEE Transactions on Medical Imaging. 2010; 29(9):1626–1635. [PubMed: 20304721]

Zhang H, Hubbard PL, Parker GJM, Alexander DC. Axon diameter mapping in the presence of orientation dispersion with diffusion mri. Neuroimage. 2011; 56(3):1301–1315. [PubMed: 21316474]

Highlights

We propose a model-based approach to estimate fibre orientation dispersion from diffusion MRI data.

The model accounts for within-voxel fibre fanning and bending.

Using extensive simulations, we demonstrate the robustness of our model against data quality.

We also compare our approach to several other non-parametric strategies.

Finally, we illustrate the fine anatomical details uncovered by this model on a high quality post-mortem macaque data set.

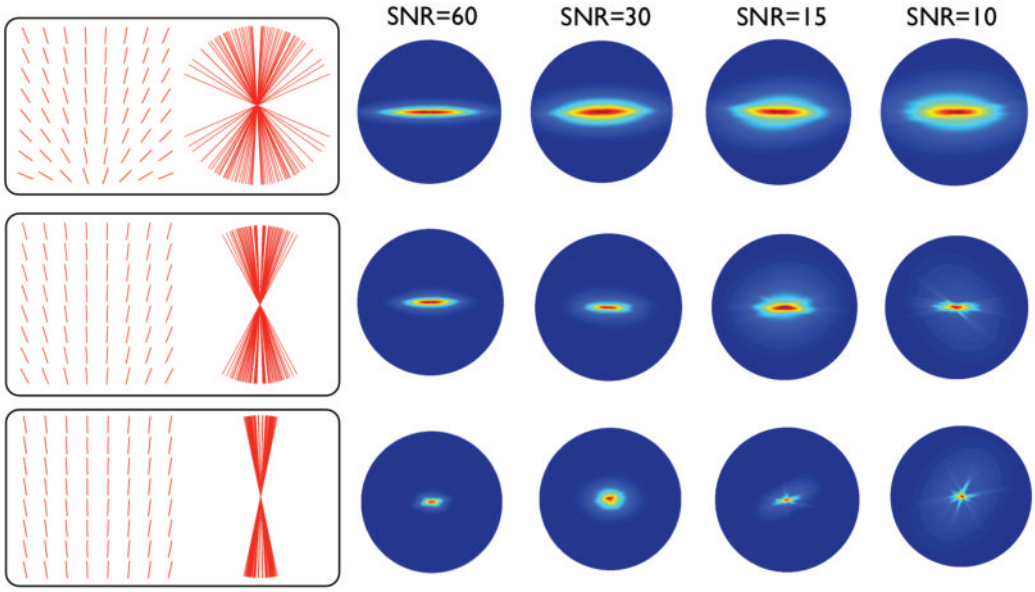

Figure 1.

Generation of signal corresponding to a fanning pattern and estimates from the ball and rackets model. Columns from left to right: Subvoxel grids used to simulate the signal from a fanning pattern, Fibre orientations of the grid grouped together, Average Bingham distribution estimated across 15 simulations for different SNR values. For better visualisation, the distributions are rotated so that the fanning plane is shown. The blue-red colour codes 0 to high values of the distribution. A b = 2000 s/mm^2 and 120 directions were used. In all cases, the fanning pattern was obtained using an anisotropic 1×8×8 grid.

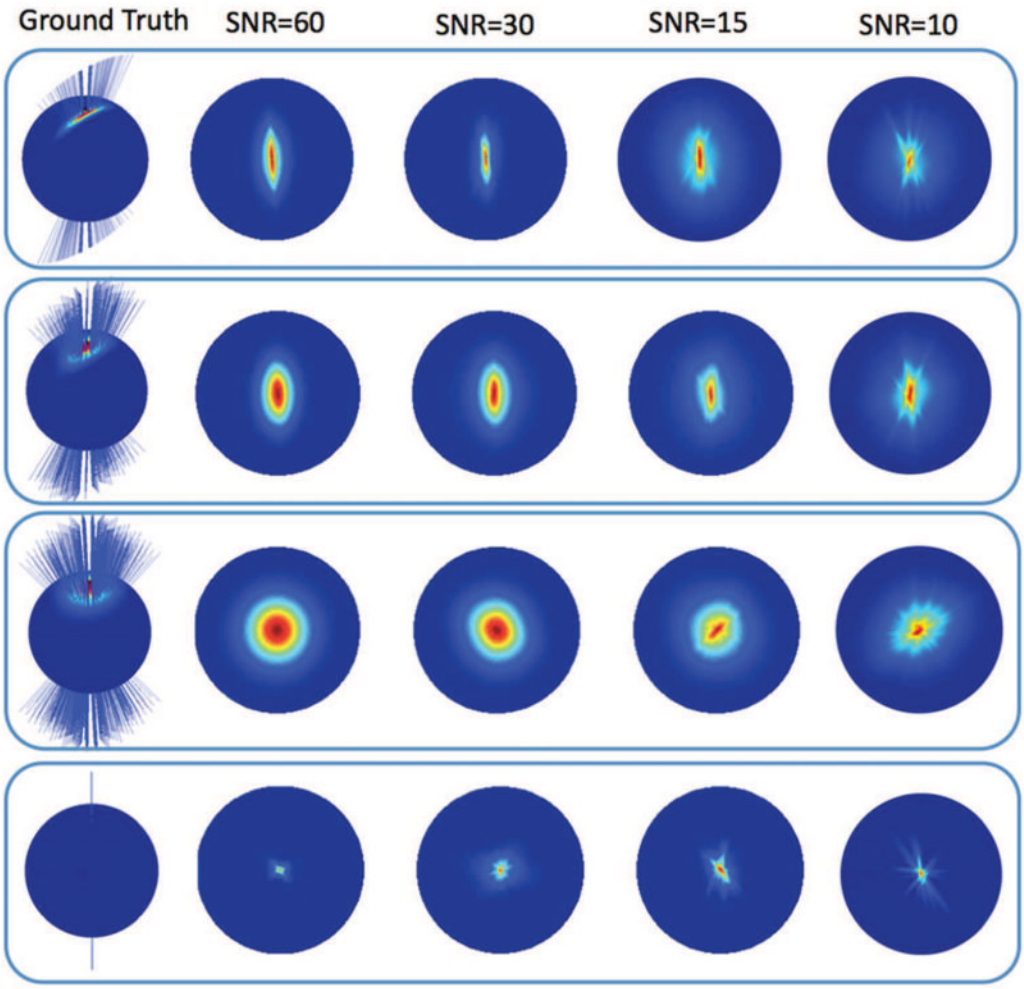

Figure 2.

Average Bingham distribution estimated across 15 simulations for four different patterns and under different SNR values. The patterns correspond (from top to bottom) to: very anisotropic (1×8×8 grid), anisotropic (4×8×8 grid), isotropic fanning (8×8×8 grid) and no fanning at all. The ground truth images show collectively all the fibre orientations present in the grid. The noise-free Bingham estimates are shown superimposed. A b = 2000 s/mm^2 and 120 directions were used for these simulations.

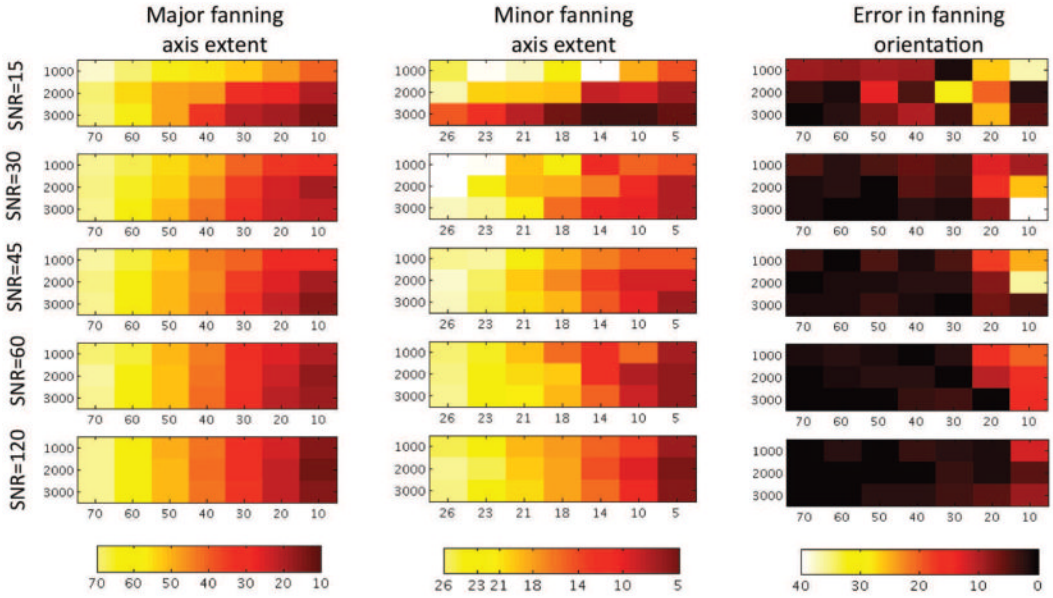

Figure 3.

Estimates of dispersion angle in degrees (95% of the distribution), along major and minor fanning axis and errors in the fanning orientation estimates (in degrees), for different acquisition parameters. The ground truth are anisotropic fanning configurations, with k_1/k_2 = 4 and the extent along the major fanning axis varied from 10 to 70 degrees. The vertical axis on each subplot represents the b value in s/mm^2 and the horizontal axis the ground truth dispersion in degrees. For each case, estimates were averaged across 15 realizations. 120 DW directions were utilized to simulate the data. The employed color-code is shown at the bottom.

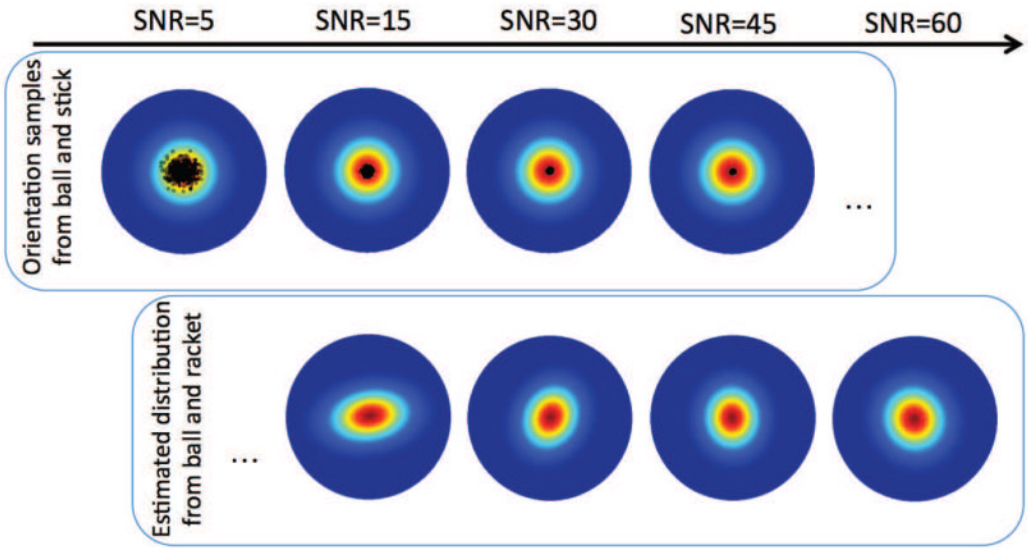

Figure 4.

Top: Orientation samples, shown as black dots, drawn using Bayesian inference and the ball and stick model on simulated datasets of an isotropic fanning pattern. Samples are shown for different SNR values, superimposed on the ground truth fanning distribution. Bottom: The estimated fanning distribution using the ball and racket model. Simulation parameters: b = 2000 s/mm^2, 60 directions.

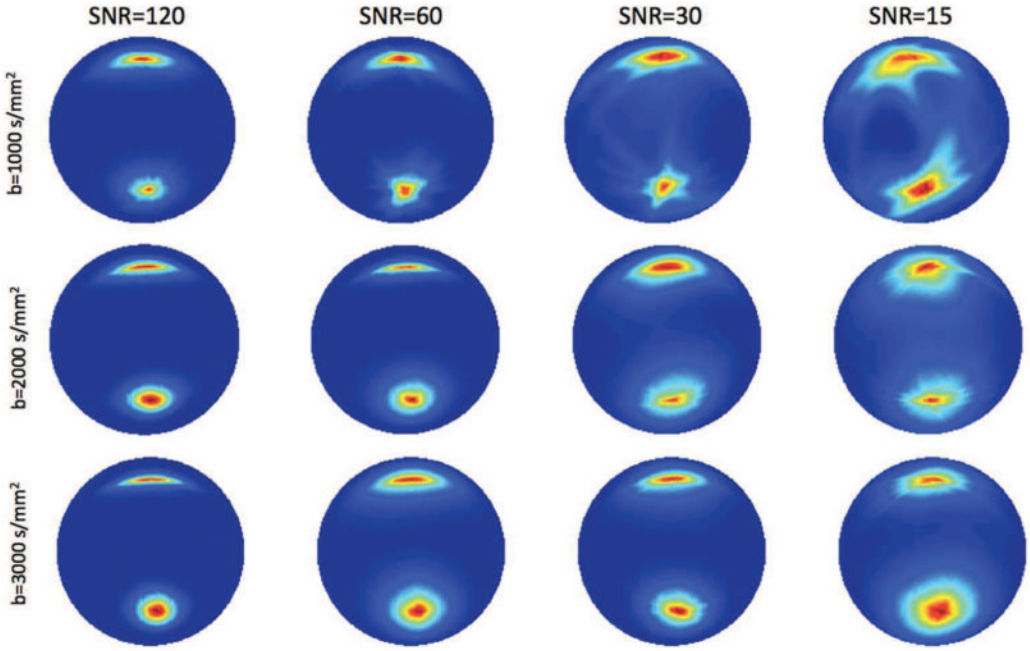

Figure 5.
Average mixture of Bingham distributions estimated across 15 simulations for a perpendicular crossing of an anisotropic and an isotropic fanning. The SNR and the *b* value is varied. 120 directions were used in this simulation and $f_1 = f_2 = 0.3$.

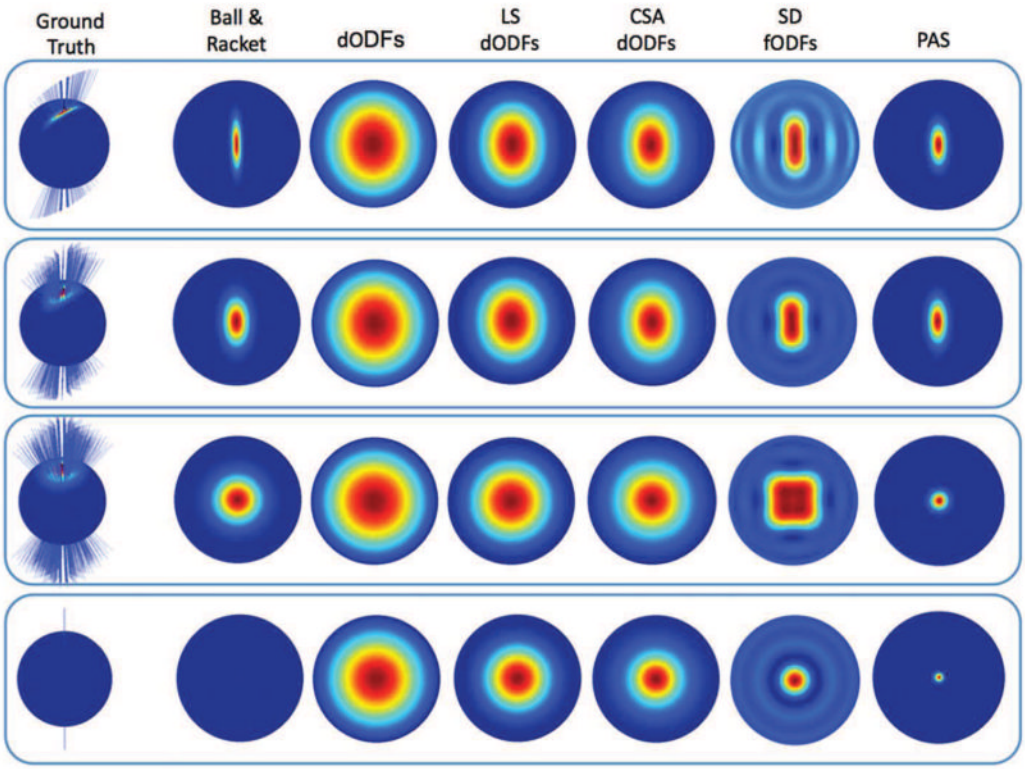

Figure 6.

Noise-free reconstructions of four fanning patterns using (from left to right): The ball and rackets model, dODFs, Laplacian-sharpened (LS) dODFs, constant solid angle (CSA) ODFs, spherical deconvolution (SD) fODFs and the persistent angular structure (PAS). The degree of fanning anisotropy was controlled by the anisotropy of the subvoxel grid: 1×8×8, 4×8×8 and 8×8×8 subvoxels were used respectively. The ground truth images show collectively all the fibre orientations present in the grid. 120 directions were used in these simulations with $b = 2000$ s/mm^2. Spherical harmonics of up to 12^{th} order were used for the ODFs. The filtering parameter for PAS was $r = 1.55$.

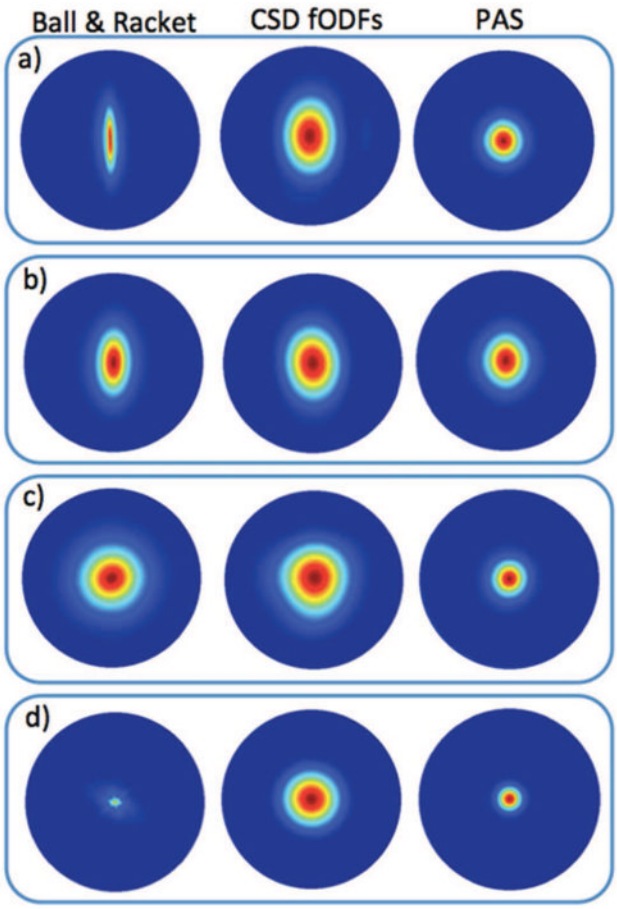

Figure 7.

Average estimates across 15 simulations of (from left to right): The ball and rackets model, CSD fODFs and the PAS, for four fanning patterns: a) Very anisotropic (1×8×8 grid), b) Anisotropic (4×8×8 grid), c) Isotropic fanning (8×8×8 grid) and d) No fanning. The SNR was 60 for these simulations. 120 directions were used with b = 2000 s/mm^2. Spherical harmonics of up to 12th order were used for CSD. The filtering parameter for PAS ws r = 1.55.

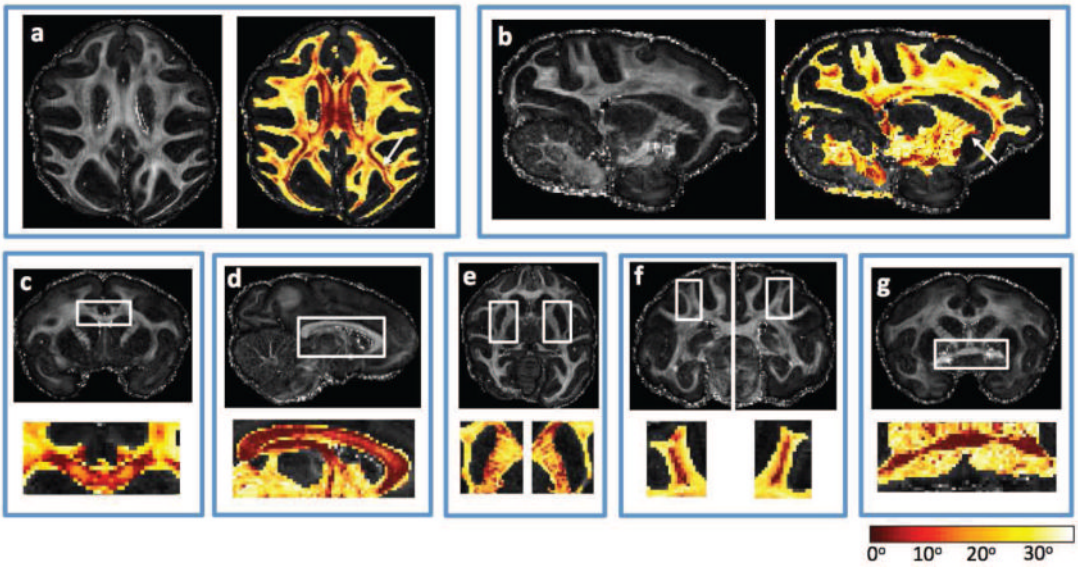

Figure 8.

Maps of mean fibre fanning extent (MF) in white matter. a) Axial slice of the anisotropic volume fraction (left) f_1 and the MF (right). MF values are shown for white matter only and are superimposed on the f_1 map. b) Sagittal slice of the f_1 and MF maps. Fanning indices in different white matter regions: c, d) Body of the corpus callosum, e) Internal capsule, f) White matter in the vicinity of cortical gyri and g) Anterior commisure. MF values in degrees are colour-coded according to the legend shown at the bottom.

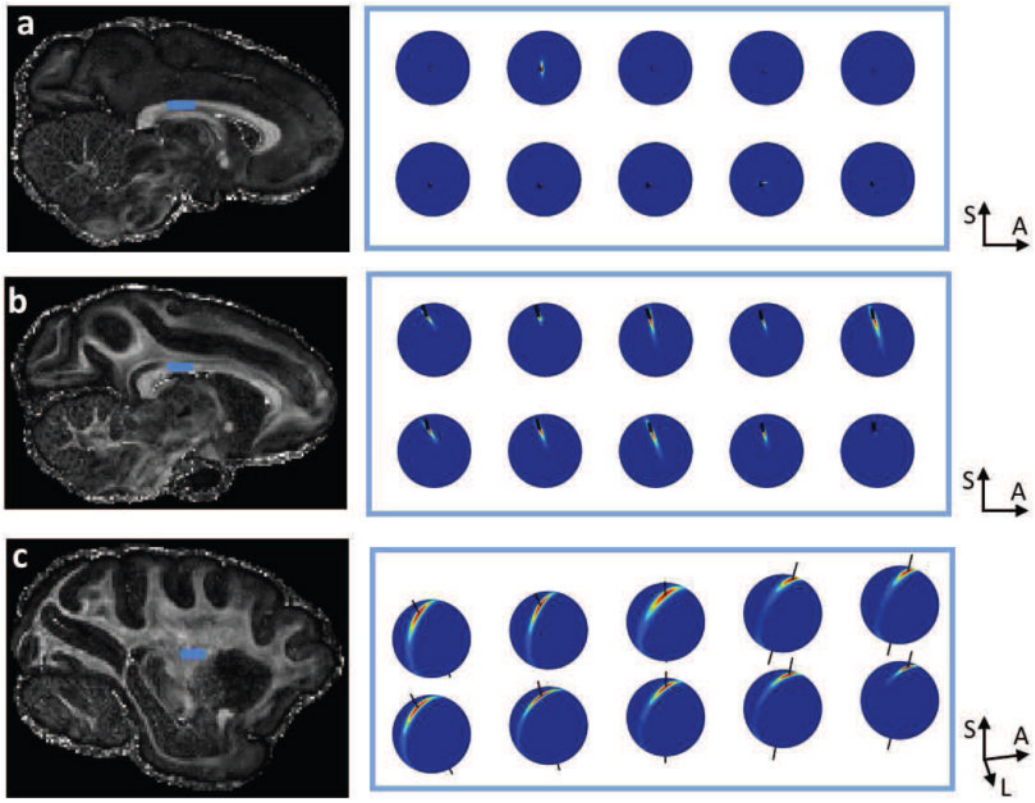

Figure 9.
Estimated fanning distributions for different white matter regions. For each voxel, the respective distribution is shown on a spherical plot. The regions from which voxels are drawn are shown with blue boxes on f_1 maps. The main fibre orientation is represented by the black line. a) Midsagittal region in the body of the corpus callosum, b) Lateral region in the body of the corpus callosum, c) Region from the posterior limb of the internal capsule. In all cases, the ball and rackets model with one fiber compartment is fitted. The coordinate system illustrates the vie angle of the spherical plots. S: Superior, A: Anterior, L: Lateral.

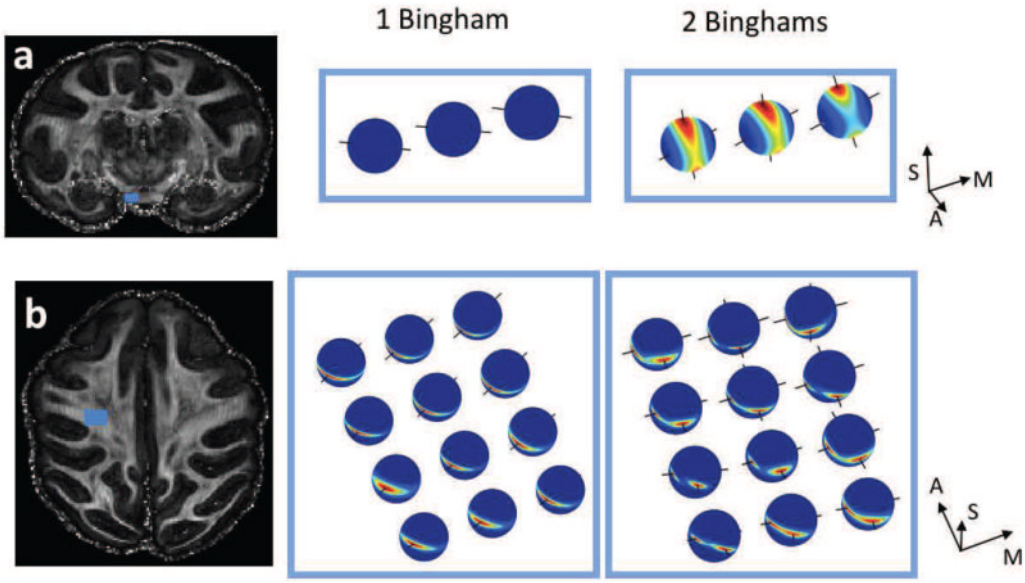

Figure 10.

Estimated fanning distributions for different white matter regions, when one or two fibre compartments are utilized in the model. For each voxel, the respective distribution is shown on a spherical plot. The regions from which voxels are drawn are shown with blue boxes on f_1 maps. The main fibre orientations are represented by black lines. a) Crossing at the pons between the corticospinal tract and the transverse pontine fibres, b) Crossing at the centrum semiovale between callosal and longitudinal fibres. The coordinate system illustrates the vie angle of the spherical plots. S: Superior, A: Anterior, M: Medial.

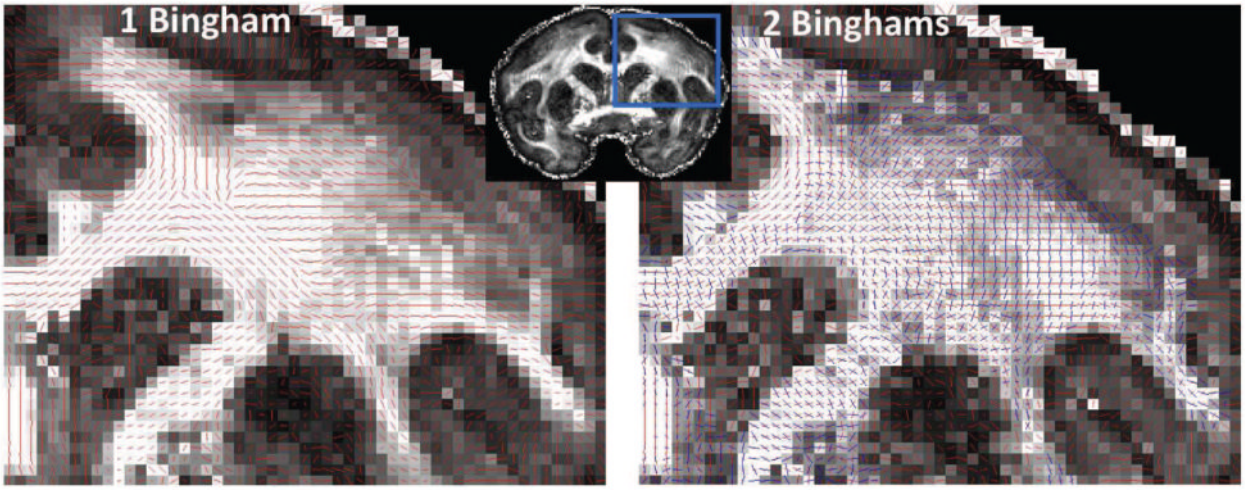

Figure 11.
Estimated fibre orientations for a region in the centrum semiovale with a one-Bingham (left) and two-Binghams (right) model. Coronal perspectives are shown. Secondary fibres are only presented in white matter to ease visualization. Orientations are superimposed on f_1 maps, estimated from the respective models.

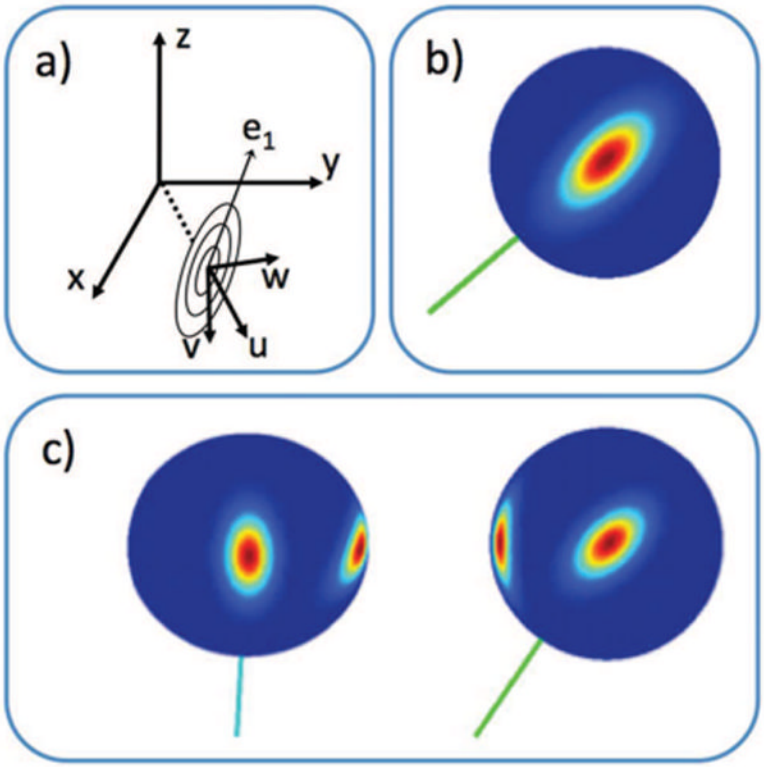

Figure 12.
Predicting fanning orientations using the ball and stick model. a) Coordinate systems utilized to project the inverse Hessian. The main fibre orientation is indicated by vector **u**. The contours show a fanning pattern on the **v-w** plane. For anisotropic fanning, the principal eigenvector e_1 of the projected inverse Hessian predicts well the fanning orientation. b, c) Anisotropic fanning shown colour-coded on the sphere and the respective prediction of the fanning orientation using this approach. Data were simulated using the ball and rackets and the ball and stick model was fitted (SNR=40). b) One fanning population, c) Two crossing fanning populations. In the crossing case, two Hessians were obtained, one for each orientation, and the respective eigenvectors predicted well the fanning orientations.

Table 1

Mean (st. deviation) across 15 simulations of the Jensen-Shannon divergence between the estimated and noise-free distribution. Simulated fanning patterns correspond to the ones presented in Figure 2.

Fanning Pattern	SNR=120	SNR=60	SNR=30	SNR=15	SNR=10
Very Anisotropic	0.0539	0.1016	0.1737	0.2887	0.3905
	(0.0558)	(0.0749)	(0.0783)	(0.112)	(0.0913)
Anisotropic	0.0128	0.055	0.0913	0.303	0.3898
	(0.0254)	(0.0949)	(0.1316)	(0.1861)	(0.1118)
Isotropic	0.0151	0.0222	0.0319	0.2509	0.3231
	(0.0452)	(0.0381)	(0.0318)	(0.2169)	(0.169)
No fanning	0.1681	0.3027	0.3117	0.3578	0.4325
	(0.1792)	(0.2123)	(0.2523)	(0.2763)	(0.2288)